High-Bandwidth and Strong Robust Current Regulation for PMLSM Drives Considering Thrust Ripple

Mingyi Wang, Liyi Li, *Member, IEEE*, Donghua Pan, Yongbin Tang, and Qingbo Guo

***Abstract*—This paper presents a high-performance current controller for the permanent-magnet linear synchronous motor considering the bandwidth and disturbances caused by the parameter variation and thrust ripple. First, an improved predictive current control (PCC) scheme based on the discretized model is proposed to increase the current control bandwidth. Besides the time-delay issue, it is noteworthy that the parameter variation in the PCC method can degrade the steady-state response. Through utilizing the information of first two sampling periods, the proposed PCC strategy can overcome such two issues at the same time. Second, a new discrete-time linearization observer is designed to estimate the thrust ripple. Then, the ripple can be suppressed by injecting the estimated value into the control system. Meanwhile, the stability analysis is given by the Lyapunov stability theory. A precise test platform based on the aerostatic guideway is established, and experimental results are shown to demonstrate the effectiveness and correctness of the proposed scheme.**

***Index Terms*—Parameter variation, permanent-magnet linear synchronous motor (PMLSM), predictive current control (PCC), thrust ripple.**

NOMENCLATURE

v_q, v_d	q- and d-axis voltages.
i_q, i_d	q- and d-axis currents.
R	Phase winding resistance.
L_q, L_d	q- and d-axis inductances.
λ_f	Permanent-magnet flux linkage.
v	Linear velocity of the mover.
d_q, d_d	q- and d-axis disturbance voltages.
T_s	Sampling period.
τ	Pole pitch.
p	Pole pairs.
m	Mass of the mover.
x	Displacement relative to the initial position.
F_e	Electromagnetic thrust.
F_l	Load thrust.
F_d	Thrust ripple.
k_f	Thrust coefficient.

Manuscript received May 21, 2015; revised August 9, 2015 and September 28, 2015; accepted November 3, 2015. Date of publication November 11, 2015; date of current version March 25, 2016. This work was supported by the Natural Science Foundation for Distinguished Young Scholars of China under Grant 51225702, by the National Natural Science Foundation of China under Grant 51177024, and by the State Key Program of National Natural Science of China under Grant 51537002. Recommended for publication by Associate Editor Y. W. Li.

M. Wang, L. Li, D. Pan, and Q. Guo are with the Department of Electrical Engineering, Harbin Institute of Technology, Harbin 150001, China (e-mail: hit_mywang@163.com; liliyi.hit@gmail.com; smile82812@163.com; azalaza2@163.com).

Y. Tang is with the Institute of Automatic Control Equipment of Beijing, Beijing 100074, China (e-mail: tangyongbin0622@163.com).

Color versions of one or more of the figures in this paper are available online at http://ieeexplore.ieee.org.

Digital Object Identifier 10.1109/TPEL.2015.2499303

I. INTRODUCTION

ALL the time, permanent-magnet linear synchronous motors (PMLSMs) with advantages of high efficiency, high force density, and fast transient response are widely applied in the precise linear motion system, such as semiconductor manufacturing equipment, precision machine tool, and robotic system [1]–[5]. Generally, the accurate and appropriate thrust regulation depends on the high-precision orientation and tracking control. For the linear motor control system, the thrust is basically controlled by the stator current. Therefore, the current control technique plays an important role in achieving the high-performance thrust output [6]–[8].

In PMLSM drives, some critical factors can affect the quality of the thrust. To ensure that the actual currents are required to track the given ones accurately and to shorten the response time as much as possible, a high-bandwidth and precise current control is essential. Though the hysteresis current control [9] with advantages of fast dynamic response and sample realization can satisfy the high-bandwidth requirement, the inconstant switching frequency brings a large current ripple. Hence, the hysteresis method is restricted in the precise control system. The main properties of proportional-integral (PI) control [10] are strong robustness and zero steady-state error, but due to the fast transient response, the overshoot issue is inevitable in the implementation. Another factor is the imperfect decoupling between *dq* axis currents [11], the coupling term impairs the performance of the thrust response. The traditional voltage feedforward decoupling control [12] can eliminate the cross coupling term of *dq* axis currents, but the parameter variations make the decoupling incomplete. The internal model control is utilized to compensate the cross coupling term in [13], which promotes the system robustness in parameter variations. However, because the compensatory voltage is calculated by the integral of the current error, the oscillation phenomenon will appear before the system achieves the steady state. Besides, the existence of back electromotive force (EMF) decreases the dynamic performance [14].

Considering the bandwidth and decoupling, the predictive current control (PCC) scheme [6]–[8] and [15], [16] based on the discretized model has a potential advantage. In theory, the

actual currents can track the required ones after one sampling period, and the tracking errors are eliminated without the overshoot. Compared with the hysteresis method, the PCC makes the best of the measured variables to reduce errors, and the switching frequency is constant. Therefore, the PCC method effectively improves the transient and static characteristics of the system. Besides, because the PCC is a model-based approach, the cross coupling term and back EMF are taken into full account. Hence, the PCC algorithm has a high decoupling effect. Precisely because of these merits, the PCC scheme is very suitable for the high-performance current regulation.

However, there are two main limitations for the PCC method. The first one is the time-delay issue, since the calculated reference voltages have one period delay in loading them to the inverter, which will lead to a large overshoot and oscillation. The second one is sensitive to the parameter uncertainties. On account of the model-based method, the PCC requires a full knowledge of motor parameters. In view of the above issues, many researchers have focused on the study of the modified PCC approaches. In [17], the delay problem is alleviated by modifying the feedback law, but multiple current references must be predicted simultaneously, which increases the difficulty of the algorithm. Due to the capability of the real-time and parallel computation, the hardware technology, such as EPROM or field programmable gate array (FPGA) solutions [18], [19], can implement the control algorithm without the sampling delay. However, a high engineering design cost makes it hard to realize the complex algorithm. In [7] and [15], the proposed method solves the delay problem through estimating currents at the next sampling time, and the actual currents reach the references after two sampling periods. For the parameter variation issue, the time-delay control approach [20] is employed to compensate the disturbance. Nevertheless, since this method requires the numerical differentiation of actual currents, a digital filer is designed to remove the high-frequency noise. In [7] and [21], the uncertainty disturbance is eliminated by using the adaptive method. However, the PCC, adaptive law, and other calculations increase the burden of the DSP controller. Additionally, many other strategies, such as model-free PCC [8], current error correction technique [22], and parameter estimation [23] or identification [24] are proposed to suppress the disturbance. Though certain good results have been obtained, the extra design enhances the complexity of the current regulation scheme.

Besides the high-current control bandwidth and strong robustness, as a parasitic force, the thrust ripple has to be suppressed in the high-accuracy PMLSM drives. Two main sources of the thrust ripple come from the slot and end effect, both of which can cause a periodic force ripple with respect to the motor position. Some structural optimization methods, such as adjusting the width of PM shifting length or pole pitch [25], designing the stator length [26], adding auxiliary poles [27], and skewing PMs [28], are studied to reduce the thrust ripple. From aspects of the flexibility and feasibility, currently the thrust ripple suppression approach has a strong trend to the control strategy. In [27], the ripple is acquired by the finite-element method (FEM), but the installation error and other uncertainties bring a certain deviation in comparison with the actual value. In [29], the compensation is implemented by using an experimental approximation. However, the rigorous test environment and auxiliary equipments are required, which makes the system complicated and inflexible. In [30], the force ripple is identified by ways of the velocity controller output, which requires the condition of the low velocity. Iterative learning control is carried out to minimize disturbances in [31]; however, this algorithm depends on some specific states, such as low velocity and repeatability of the movement. Because of the periodic disturbance, the repetitive control is exploited to decrease the low- and high-frequency harmonics in [32]. Nevertheless, this scheme spends a lot of time to reach the steady state. Considering the deficiencies of the FEM analysis and experimental identification, some researchers extract the thrust ripple through the observer-based technology. In [33], ripple components of the hybrid stepping motor are obtained by the observer, and in [34], the ripple can be obviously suppressed by a disturbance observer.

The purpose of this paper is to propose a high-performance current regulation scheme for the PMLSM drive. To realize the high bandwidth and decoupling of the current loop, the predictive control method is adopted. Due to the time delay and parameter variation in the PCC, an optimal method is presented to simultaneously overcome these two issues. The voltage and current variables of first two sampling periods are utilized to calculate the voltage command of the next period, and in this way, the time-delay problem is resolved. In the meantime, the parameter disturbance can be eliminated, since the previous variables include the information of the disturbance, thus the current loop has a strong robustness. In addition, a discrete-time linearization observer is designed to suppress the thrust ripple, and as a part of the controller, the convergence of estimated error is analyzed by the Lyapunov stability theory. This paper is organized as follows. Section II describes the overall control system and gives the PMLSM model. In Section III, the optimal PCC with the time delay and parameter variation compensation is presented. In Section IV, the discrete-time linearization observer is deduced. In Section V, the explored approach is validated by experiments. Finally, the conclusion is given in Section VI.

II. Current Control System

A. System Description

The overall block diagram of the proposed control scheme for the PMLSM drive is depicted in Fig. 1. Generally, a high-performance linear motor drive system is composed of the position loop, velocity loop, and current loop. As the inner part, the current loop plays a significant role in the drive system. Therefore, the current regulation scheme has to consider various influences, such as bandwidth, decoupling, robustness, and ripple suppression. The original current command is given by the output of the velocity controller. Through the improved PCC and thrust ripple compensation method, the voltage command is achieved by the proposed current regulation scheme. Combined with the space vector pulse width modulation technique, the voltage command can be loaded to the PMLSM by a three-phase voltage source inverter (VSI).

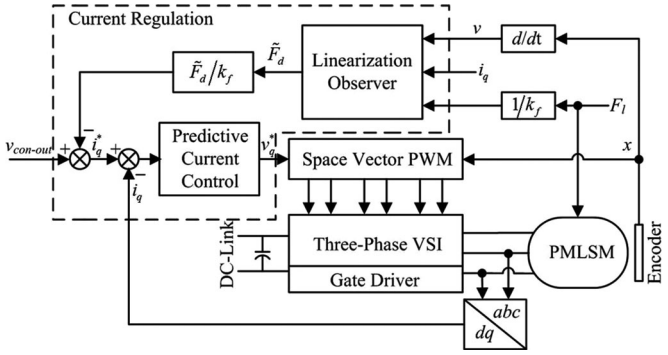

Fig. 1. Block diagram of the proposed control scheme.

B. Modeling of the PMLSM With the Parameter Variation

Neglecting the flux distortions, the voltage equations of the *dq* frame are expressed by

$$\begin{cases} v_q = R_o i_q + \dfrac{d\lambda_{qo}}{dt} + \dfrac{\pi v \lambda_{do}}{\tau} + d_q \\ v_d = R_o i_d + \dfrac{d\lambda_{do}}{dt} - \dfrac{\pi v \lambda_{qo}}{\tau} + d_d \end{cases} \tag{1}$$

where $\lambda_{qo} = L_{qo} i_q, \lambda_{do} = L_{do} i_d + \lambda_{fo}$, and the subscript "$o$" denotes the nominal value.

The disturbance voltages on the parameter variation can be represented by d_q, d_d, which are given as

$$\begin{cases} d_q = \Delta R i_q + \dfrac{\Delta L_q di_q}{dt} + \dfrac{\pi v \Delta L_d i_d}{\tau} + \dfrac{\pi v \Delta \lambda_f}{\tau} \\ d_d = \Delta R i_d + \dfrac{\Delta L_d di_d}{dt} - \dfrac{\pi v \Delta L_q i_q}{\tau}. \end{cases} \tag{2}$$

The discrete-time equations of (1) can be described as

$$\begin{cases} v_q(k) = R_o i_q(k) + \dfrac{L_{qo}}{T_s}\left[i_q(k+1) - i_q(k)\right] \\ \qquad + \dfrac{\pi v L_{do}}{\tau} i_d(k) + \dfrac{\pi v \lambda_{fo}}{\tau} + d_q(k) \\ v_d(k) = R_o i_d(k) + \dfrac{L_{do}}{T_s}\left[i_d(k+1) - i_d(k)\right] \\ \qquad - \dfrac{\pi v L_{qo}}{\tau} i_q(k) + d_d(k). \end{cases} \tag{3}$$

The dynamic equations of (3) can be represented as the following state-space form

$$\tilde{\mathbf{V}}(k) = \tilde{\mathbf{G}} \cdot \tilde{\mathbf{I}}(k) + \tilde{\mathbf{H}} \cdot \tilde{\mathbf{I}}(k+1) + \tilde{\lambda} + \tilde{\mathbf{D}}(k) \tag{4}$$

where

$$\tilde{\mathbf{V}}(k) = \begin{bmatrix} v_q(k) & v_d(k) \end{bmatrix}^T, \quad \tilde{\mathbf{I}}(k) = \begin{bmatrix} i_q(k) & i_d(k) \end{bmatrix}^T,$$
$$\tilde{\lambda} = \begin{bmatrix} \pi v \lambda_{fo}/\tau & 0 \end{bmatrix}^T, \quad \tilde{\mathbf{D}}(k) = \begin{bmatrix} d_q(k) & d_d(k) \end{bmatrix}^T$$
$$\tilde{\mathbf{G}} = \begin{bmatrix} R_o - L_{qo}/T_s & \pi v L_{do}/\tau \\ -\pi v L_{qo}/\tau & R_o - L_{do}/T_s \end{bmatrix},$$
$$\tilde{\mathbf{H}} = \begin{bmatrix} L_{qo}/T_s & 0 \\ 0 & L_{do}/T_s \end{bmatrix}.$$

III. Optimal PCC Scheme

For the conventional PCC, during the *k*th period, the voltage command $\tilde{\mathbf{V}}^*(k)$ can be achieved by (4). The equation can be rewritten as

$$\tilde{\mathbf{V}}^*(k) = \tilde{\mathbf{G}} \cdot \tilde{\mathbf{I}}(k) + \tilde{\mathbf{H}} \cdot \tilde{\mathbf{I}}^*(k+1) + \tilde{\lambda} + \tilde{\mathbf{D}}(k) \tag{5}$$

where the subscript "$*$" denotes the command value.

If the disturbance vector $\tilde{\mathbf{D}}(k)$ is known, ideally, the command $\tilde{\mathbf{I}}^*(k+1)$ is tracked after one sampling period. However, because of the implemented delay, the command $\tilde{\mathbf{V}}^*(k)$ is loaded to the inverter at the next period. As a result, an overshoot or even oscillation phenomenon maybe appears. Therefore, in [7] and [15], the control voltage of the $(k+1)$th period is obtained on the basis of (5) as follows:

$$\tilde{\mathbf{V}}^*(k+1) = \tilde{\mathbf{G}} \cdot \tilde{\mathbf{I}}_\eta(k+1) + \tilde{\mathbf{H}} \cdot \tilde{\mathbf{I}}^*(k+2) + \tilde{\lambda} + \tilde{\mathbf{D}}(k+1) \tag{6}$$

where $\tilde{\mathbf{I}}_\eta(k+1)$ is the estimated current vector at the $(k+1)$th sampling instant, which can be given as

$$\tilde{\mathbf{I}}_\eta(k+1) = \tilde{\mathbf{H}}^{-1} \cdot \left\{ \tilde{\mathbf{V}}(k) - \tilde{\mathbf{G}} \cdot \tilde{\mathbf{I}}(k) - \tilde{\lambda} - \tilde{\mathbf{D}}(k) \right\}. \tag{7}$$

Substituting (7) into (6), the vector $\tilde{\mathbf{V}}^*(k+1)$ can be rewritten as

$$\begin{aligned} \tilde{\mathbf{V}}^*(k+1) = {} & \tilde{\mathbf{G}} \cdot \tilde{\mathbf{H}}^{-1} \cdot \left\{ \tilde{\mathbf{V}}(k) - \tilde{\mathbf{G}} \cdot \tilde{\mathbf{I}}(k) - \tilde{\lambda} - \tilde{\mathbf{D}}(k) \right\} \\ & + \tilde{\mathbf{H}} \cdot \tilde{\mathbf{I}}^*(k+2) + \tilde{\lambda} + \tilde{\mathbf{D}}(k+1). \end{aligned} \tag{8}$$

If disturbance vectors remain unchanged during two adjacent sampling periods, the vector $\tilde{\mathbf{V}}^*(k+1)$ is the function of the voltage, current, and disturbance vector at the *k*th sampling time. When the vector $\tilde{\mathbf{V}}^*(k+1)$ is loaded to PMLSM during the $(k+1)$th period, the reference current vector $\tilde{\mathbf{I}}^*(k+2)$ will be tracked at the end of the $(k+2)$th period.

According to the above derivation, the time-delay issue will be overcome if the disturbance is known. Nevertheless, the parameters are uncertain, which impairs the robustness of the control system. Recently, many methods devote to compensate this disturbance through different types of observers or the adaptive approach, but those ways complicate the PCC strategy. This paper focuses on a simple and novel method which deals with the time delay and parameter variation issues at the same time.

Fig. 2 shows the schematic diagram of the proposed PCC method. We regard two sampling periods as one control period, which means

$$\begin{cases} \tilde{\mathbf{I}}(m-1) = \tilde{\mathbf{I}}(k-2) \\ \tilde{\mathbf{I}}(m) = \tilde{\mathbf{I}}(k) \\ \tilde{\mathbf{I}}(m+1) = \tilde{\mathbf{I}}(k+2). \end{cases} \tag{9}$$

According to (4), the discrete-time voltage equations in the *m*th and $(m-1)$th control period can be expressed as

$$\begin{cases} \tilde{\mathbf{V}}^*(m) = \tilde{\mathbf{G}}_1 \cdot \tilde{\mathbf{I}}(m) + \tilde{\mathbf{H}}_1 \cdot \tilde{\mathbf{I}}^*(m+1) + \tilde{\lambda} + \tilde{\mathbf{D}}(m) \\ \tilde{\mathbf{V}}(m-1) = \tilde{\mathbf{G}}_1 \cdot \tilde{\mathbf{I}}(m-1) + \tilde{\mathbf{H}}_1 \cdot \tilde{\mathbf{I}}(m) + \tilde{\lambda} + \tilde{\mathbf{D}}(m-1) \end{cases} \tag{10}$$

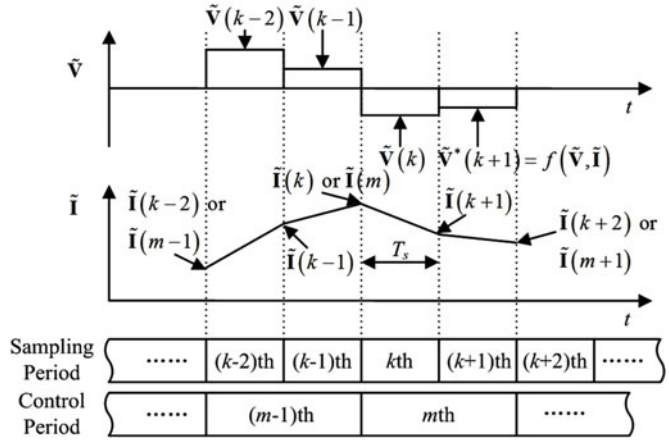

Fig. 2. Schematic diagram of the proposed PCC method.

where

$$\tilde{\mathbf{G}}_1 = \begin{bmatrix} R_o - L_{qo}/(2T_s) & \pi v L_{do}/\tau \\ -\pi v L_{qo}/\tau & R_o - L_{do}/(2T_s) \end{bmatrix},$$

$$\tilde{\mathbf{H}}_1 = \begin{bmatrix} L_{qo}/(2T_s) & 0 \\ 0 & L_{do}/2T_s \end{bmatrix} \quad \tilde{\mathbf{V}}(m),$$

is the average voltage between the *k*th and $(k+1)$th sampling period, and defined as

$$\begin{cases} \tilde{\mathbf{V}}^*(m) = \dfrac{\tilde{\mathbf{V}}(k) + \tilde{\mathbf{V}}^*(k+1)}{2} \\ \tilde{\mathbf{V}}(m-1) = \dfrac{\tilde{\mathbf{V}}(k-2) + \tilde{\mathbf{V}}(k-1)}{2}. \end{cases} \tag{11}$$

Generally, compared with the parameter disturbance, the control frequency is so fast that two adjacent disturbance vectors approximately remain the same, which is written as

$$\tilde{\mathbf{D}}(m) = \tilde{\mathbf{D}}(m-1). \tag{12}$$

Making a subtraction between two voltage equations in (10), according to (12), the disturbance vector term can be removed, which can be expressed as

$$\begin{aligned} \tilde{\mathbf{V}}^*(m) = {} & \tilde{\mathbf{G}}_1 \cdot \left[\tilde{\mathbf{I}}(m) - \tilde{\mathbf{I}}(m-1)\right] + \tilde{\mathbf{H}}_1 \cdot \left[\tilde{\mathbf{I}}^*(m+1)\right. \\ & \left. -\tilde{\mathbf{I}}(m)\right] + \tilde{\mathbf{V}}(m-1). \end{aligned} \tag{13}$$

Substituting (9) and (11) into (13), the final control voltage is deduced as

$$\begin{aligned} \tilde{\mathbf{V}}^*(k+1) = {} & 2\tilde{\mathbf{G}}_1 \cdot \left\{\tilde{\mathbf{I}}(k) - \tilde{\mathbf{I}}(k-2)\right\} \\ & + 2\tilde{\mathbf{H}}_1 \cdot \left\{\tilde{\mathbf{I}}^*(k+2) - \tilde{\mathbf{I}}(k)\right\} \\ & + \tilde{\mathbf{V}}(k-2) + \tilde{\mathbf{V}}(k-1) - \tilde{\mathbf{V}}(k). \end{aligned} \tag{14}$$

Compared with (5), the reference voltage vector acquired in (14) is similar to that in (8), it is the calculated value of the $(k+1)$th period, thus the overshoot and oscillation caused by the time delay can be eliminated. In (14), it is clear that the terms about $\tilde{\lambda}$ and $\tilde{\mathbf{D}}(k)$ are removed, and the control voltage is merely associated with voltage and current variables of first two sampling periods, hence the control robustness is improved. Eventually, the optimal PCC method overcomes the delay issue; meanwhile, the disturbance produced by the parameter variation is suppressed.

IV. Thrust Ripple Compensation

The high-performance current regulation not only requires a high-bandwidth and strong robust current control strategy, but also can compensate the parasitic thrust ripple. To decrease the ripple, an appropriate compensation method should be studied in the system. This section presents a discrete-time linearization observer under the condition of the velocity closed-loop control. Then, the observed ripple force is injected into the controller in the form of the feedforward.

A. Linearization Observer Scheme

Due to the surface mounted structure of PMLSM, we can assume $L_{qo} = L_{do} = L_{so}$. Based on the field oriented control method with $i_d = 0$, the electromagnetic thrust F_e is expressed as

$$F_e = k_f i_q \tag{15}$$

where $k_f = 3\pi p \lambda_f / 2\tau$.

As a parasitic force, the thrust force changes periodically with the motor position. Therefore, the thrust ripple can be written as Fourier series

$$F_d = \sum_{n=1}^{\infty} f_n \cos\left(\frac{n\pi}{\tau}x + \delta_n\right) \tag{16}$$

where f_n and δ_n are the amplitude and initial electrical angle of the *n*th order harmonic, respectively.

Ignoring the frictional and cable disturbance force, the motion equation of PMLSM is given as

$$F_e + F_d = m\frac{dv}{dt} + F_l. \tag{17}$$

To observe the ripple, first, a state vector is set as

$$\mathbf{x} = [x_1, x_2, x_3, \cdots, x_{2n}, x_{2n+1}]^T \quad (n = 1, 2, \cdots) \tag{18}$$

where elements in the state vector can be defined as

$$\begin{aligned} x_1 &= v \\ x_2 &= f_1 \cos\left(\frac{\pi}{\tau}x + \delta_1\right) \\ x_3 &= -\frac{f_2 \tau}{2\pi} \sin\left(\frac{2\pi}{\tau}x + \delta_2\right) \\ &\vdots \\ x_{2n} &= f_n \cos\left(\frac{n\pi}{\tau}x + \delta_n\right) \\ x_{2n+1} &= -\frac{f_n \tau}{n\pi} \sin\left(\frac{n\pi}{\tau}x + \delta_n\right). \end{aligned} \tag{19}$$

It is seen in (19) that the ripple force can be expressed as the sum of $x_2, x_4, \ldots, x_{2n}$, which means

$$F_d = \sum_{i=1}^{n} x_{2i}. \tag{20}$$

Substituting (15), (19), and (20) into (17), the derivative of velocity is written as

$$\dot{x}_1 = \frac{dv}{dt} = \frac{1}{m}\left[k_f\left(i_q - i_{ql}\right) + \sum_{i=1}^{n} x_{2i}\right] \tag{21}$$

where i_{ql} is the q-axis current corresponding to the load thrust.

Besides x_1, the derivatives of other terms in (19) are deduced as

$$\begin{aligned} \dot{x}_2 &= \left(\frac{\pi}{\tau}\right)^2 x_1 x_3 \\ \dot{x}_3 &= -x_1 x_2 \\ &\vdots \\ \dot{x}_{2n} &= \left(\frac{n\pi}{\tau}\right)^2 x_1 x_{2n+1} \\ \dot{x}_{2n+1} &= -x_1 x_{2n}. \end{aligned} \tag{22}$$

Uniting (21) and (22), the overall state equation is expressed as

$$\begin{cases} \dot{\mathbf{x}} = F(\mathbf{x}) + G(\mathbf{x})\, u \\ \mathbf{y} = H(\mathbf{x}) \end{cases} \tag{23}$$

where

$$\begin{aligned} F(\mathbf{x}) &= \begin{bmatrix} \frac{1}{m}\sum_{i=1}^{n} x_{2i} \\ \left(\frac{\pi}{\tau}\right)^2 x_1 x_3 \\ -x_1 x_2 \\ \vdots \\ \left(\frac{n\pi}{\tau}\right)^2 x_1 x_{2n+1} \\ -x_1 x_{2n} \end{bmatrix}_{(2n+1)\times 1} \qquad G(\mathbf{x}) = \begin{bmatrix} \frac{1}{m} \\ 0 \\ 0 \\ \vdots \\ 0 \\ 0 \end{bmatrix}_{(2n+1)\times 1} \\ H(\mathbf{x}) &= x_1 \qquad\qquad u = k_f\left(i_q - i_{ql}\right). \end{aligned} \tag{24}$$

It is clear that (23) is a nonlinear state equation. In the linear system, the nonlinear observer is hard to be implemented. Hence, some researchers deal with this problem through the approximate linearization approach. This paper adopts Jacobian linearization observer [33] and [35], the state vector is redefined as

$$\tilde{\mathbf{x}} = [\tilde{x}_1, \tilde{x}_2, \tilde{x}_3, \cdots, \tilde{x}_{2n}, \tilde{x}_{2n+1}]^T \quad (n = 1, 2, \cdots). \tag{25}$$

To acquire the linear state equation, based on (21) and (22), the derivative of the state vector can be rewritten as

$$\begin{aligned} \dot{\tilde{x}}_1 &= \frac{1}{m}\left[k_f\left(i_q - i_{ql}\right) + \sum_{i=1}^{n} \tilde{x}_{2i}\right] + k_1\left(v - \tilde{x}_1\right) \\ \dot{\tilde{x}}_2 &= \left(\frac{\pi}{\tau}\right)^2 v\tilde{x}_3 + k_2\left(v - \tilde{x}_1\right) \\ \dot{\tilde{x}}_3 &= -v\tilde{x}_2 \\ &\vdots \\ \dot{\tilde{x}}_{2n} &= \left(\frac{n\pi}{\tau}\right)^2 v\tilde{x}_{2n+1} + k_{n+1}\left(v - \tilde{x}_1\right) \\ \dot{\tilde{x}}_{2n+1} &= -v\tilde{x}_{2n}. \end{aligned} \tag{26}$$

Therefore, the linear state equation can be expressed as

$$\begin{cases} \dot{\tilde{\mathbf{x}}} = F(\tilde{\mathbf{x}}) + G(\tilde{\mathbf{x}})\, u \\ \tilde{\mathbf{y}} = H(\tilde{\mathbf{x}}) \end{cases} \tag{27}$$

where

$$\begin{aligned} F(\tilde{\mathbf{x}}) &= \begin{bmatrix} \frac{1}{m}\sum_{i=1}^{n} \tilde{x}_{2i} + k_1\left(v - \tilde{x}_1\right) \\ \left(\frac{\pi}{\tau}\right)^2 v\tilde{x}_3 + k_2\left(v - \tilde{x}_1\right) \\ -v\tilde{x}_2 \\ \vdots \\ \left(\frac{n\pi}{\tau}\right)^2 v\tilde{x}_{2n+1} + k_{n+1}\left(v - \tilde{x}_1\right) \\ -v\tilde{x}_{2n} \end{bmatrix}_{(2n+1)\times 1} \\ G(\tilde{\mathbf{x}}) &= \begin{bmatrix} \frac{1}{m} \\ 0 \\ 0 \\ \vdots \\ 0 \\ 0 \end{bmatrix}_{(2n+1)\times 1} \qquad H(\tilde{\mathbf{x}}) = \tilde{x}_1 \end{aligned} \tag{28}$$

where $\mathbf{K} = [k_1, k_2, \cdots, k_{n+1}]^T \ \ (n = 1, 2, \cdots)$ is chosen such that $(\partial\mathbf{F}/\partial\mathbf{x})(0) + \mathbf{K}(\partial\mathbf{H}/\partial\mathbf{x})(0)$ is a Hurwitz matrix [35].

According to the definition of the thrust ripple in (20), the observed ripple can be redefined as

$$\tilde{F}_d = \sum_{i=1}^{n} \tilde{x}_{2i}. \tag{29}$$

Based on the derivation above, the estimated thrust ripple can be obtained by the designed linearization observer, and the compensation current is injected into the control system in the form of the feedforward. The detail control block diagram is shown as Fig. 3.

B. Lyapunov Stability Analysis

Since the current loop includes the thrust ripple compensation, if the observer is directly used, the control system cannot guarantee the stability. Therefore, the stability analysis is indispensable. Equation (20) is a reference equation, which represents an ideal thrust ripple, and (29) is an estimated equation, therefore the estimated error vector is defined as

$$\mathbf{e} = \mathbf{x} - \tilde{\mathbf{x}} \tag{30}$$

where $\mathbf{e} = [\mathbf{e_1}, \mathbf{e_2}, \ldots, \mathbf{e_{2n+1}}]^{\mathbf{T}}$. By subtracting (27) from (23), the error dynamics can be calculated as

$$\begin{aligned}
\dot{e}_1 &= \frac{1}{m}\sum_{i=1}^{n} e_{2i} - k_1 e_1 \\
\dot{e}_2 &= \left(\frac{\pi}{\pi}\right)^2 v e_3 - k_2 e_1 \\
\dot{e}_3 &= -v e_2 \\
&\vdots \\
\dot{e}_{2n} &= \left(\frac{n\pi}{\pi}\right)^2 v e_{2n+1} - k_{2+1} e_1 \\
\dot{e}_{2n+1} &= -v e_{2n}.
\end{aligned} \tag{31}$$

The dynamic equations of (31) can be expressed as the state-space form

$$\dot{\mathbf{e}} = \mathbf{A}\cdot\mathbf{e} \tag{32}$$

$$\mathbf{A} = \begin{bmatrix}
-k_1 & \frac{1}{m} & 0 & \cdots & \frac{1}{m} & 0 \\
-k_2 & 0 & \left(\frac{\pi}{\tau}\right)^2 v & \cdots & 0 & 0 \\
0 & -v & 0 & \cdots & 0 & 0 \\
\vdots & \vdots & \vdots & \vdots & \vdots & \vdots \\
-k_{n+1} & 0 & 0 & \cdots & 0 & \left(\frac{n\pi}{\tau}\right)^2 v \\
0 & 0 & 0 & \cdots & -v & 0
\end{bmatrix}_{(2n+1)\times(2n+1).} \tag{33}$$

To make the designed observer stable, the following objective should be meet: $\lim_{t\to\infty} \mathbf{e}(t) = 0$ for any initial condition $\mathbf{e}(0)$. Therefore, the Lyapunov stability theory is used to deduce the satisfied conditions. The Lyapunov function is defined as

$$V = \mathbf{e}^T \mathbf{P} \mathbf{e} \tag{34}$$

where $\mathbf{P}$ is a $(2n+1)\times(2n+1)$ symmetric positive-definite matrix, and can be given as

$$\mathbf{P} = \operatorname{diag}\left(\frac{1}{2}\rho m, \frac{1}{2}, \frac{1}{2}\left(\frac{\pi}{\tau}\right)^2, \cdots, \frac{1}{2}, \frac{1}{2}\left(\frac{n\pi}{\tau}\right)^2\right)_{(2n+1)\times(2n+1)} \tag{35}$$

where ρ is a constant. The derivative of (34) can be expressed as

$$\dot{V} = \dot{\mathbf{e}}^T \mathbf{P} \mathbf{e} + \mathbf{e}^T \mathbf{P} \dot{\mathbf{e}} = -\mathbf{e}^T \mathbf{Q} \mathbf{e} \tag{36}$$

where Q is a symmetric positive definite matrix and can be given as

$$\mathbf{A}^T \mathbf{P} + \mathbf{P}\mathbf{A} = -\mathbf{Q}. \tag{37}$$

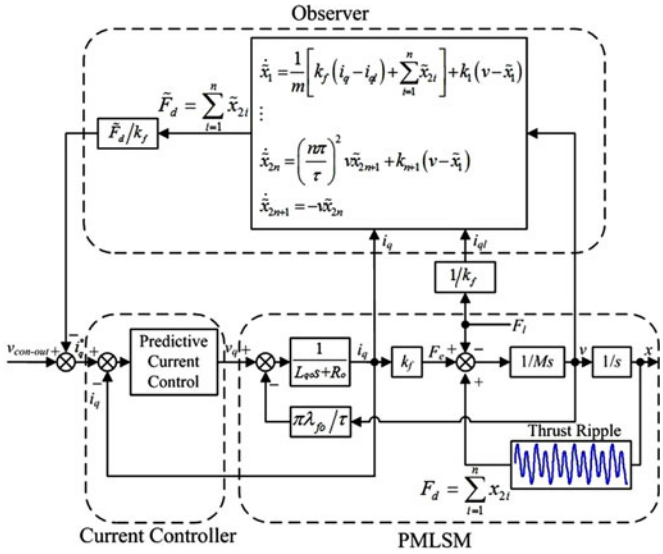

Fig. 3. Block diagram of the thrust ripple compensation.

Substituting (33), (35), and (37) into (36), (36) can be rewritten as

$$\dot{V} = -\rho m k_1 e_1^2 + \sum_{i=1}^{n} \left(\left(\rho - k_{i+1}\right) e_1 e_{2i}\right). \tag{38}$$

If the following conditions are satisfied:

1) the constant ρ has a positive value ($\rho > 0$);
2) $k_1 > 0$ and $k_{i+1} = \rho (i = 1, \ldots, n)$.

Then, the derivation of the Lyapunov function can be deduced as

$$\dot{V} = -\rho k_1 m e_1^2 < 0. \tag{39}$$

This proves that the linear model in (27) asymptotically stabilizes to the nonlinear one in (23); thus, the designed observer can be utilized to suppress the thrust ripple without affecting the stability of the current loop.

V. Experimental Results

Fig. 4 illustrates the overall experimental platform of the PMLSM system. The linear motor adopts the skewed permanent-magnet structure, which can suppress the thrust ripple. To measure the ripple force, an air bearing test platform is established to remove the friction, and the air pressure provided for the air bearing is 400 kPa. As an auxiliary test motor, the servo rotary motor with a precision ball screw unit is used to drive the linear motor in a constant velocity, and to test the thrust ripple through using a precise force sensor. The servo rotary motor and controller are manufactured by YASKAWA. The ball screw unit is produced by THK with the length of 1.6 m. The ripple is measured by a force sensor with the rated load of 100 N.The position of the linear motor is measured by a Renishaw linear incremental encoder with the effective resolution of 0.1 μm. The motor is driven by a full-digital power amplifier based on the FPGA. The amplifier adopts a VSI with three sets of insulated-gate bipolar transistors. The bus voltage is 70 V and the switching frequency is 5 kHz. Three LEM current sensors

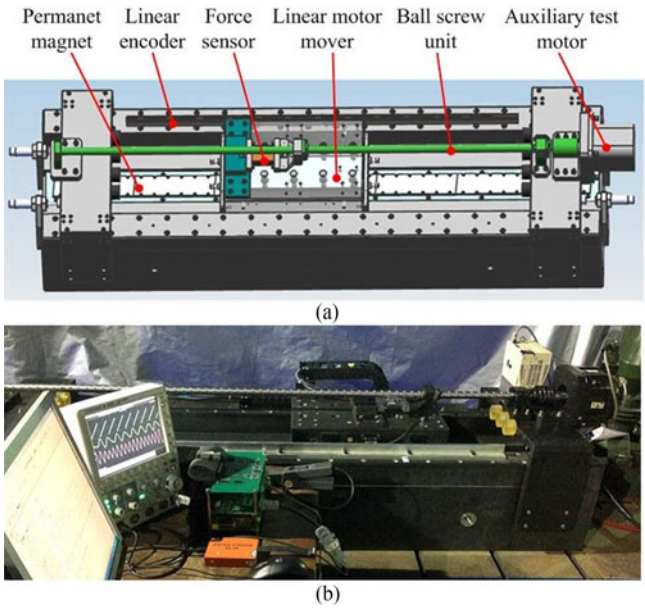

Fig. 4. Experimental platform of the PMLSM system. (a) Structure diagram. (b) System image.

TABLE I
MAIN PARAMETERS OF THE PMLSM

Parameters	Values	Unit
Rated force	450	N
Maximum force	1250	N
Stator resistance	4.2	Ω
Stator inductance	28.5	mH
Mover mass	45	Kg
Pole pitch	12	mm
Thrust coefficient	98	N/A
Magnetic flux	0.12	Wb

with the primary nominal current of 25 A and the accuracy of $\pm 0.2\%$ are utilized. A dual 16-bit AD converter with four fully differential input channels is used. To carry out the proposed control strategy, the algorithm is realized by using Turbo C language on a TMS320F2808 DSP controller. The internal data of DSP are displayed through a 12-bit digital-to-analog converter with eight channels. The main parameters of the motor are listed in Table I.

To express the superiority of the proposed PCC, a PI control method is used as a comparison. Fig. 5 shows the test results of PI control with different proportional (K_P) and integral (K_I) gains, and the Table II gives the corresponding PI parameters of different curves. The q-axis current command i_q^* is a square wave with the amplitude of 1.25 A and the period of 80 ms. The actual current $i_{q1}(K_P = 5, K_I = 0.1)$ just has a small overshoot, and can be seen as an optimal tracking result for PI control. In Fig. 5, if K_I remains the same, i_{q2} and i_{q3} are the tracking results when K_P decreases and increases, respectively. It is clear that the proportional gain K_P affects the dynamic response performance. When K_P is large enough, the system will be unstable, such as i_{q3}. In addition, if K_P remains the same, i_{q4} and i_{q5} are the tracking results when K_I decreases and increases, respectively.

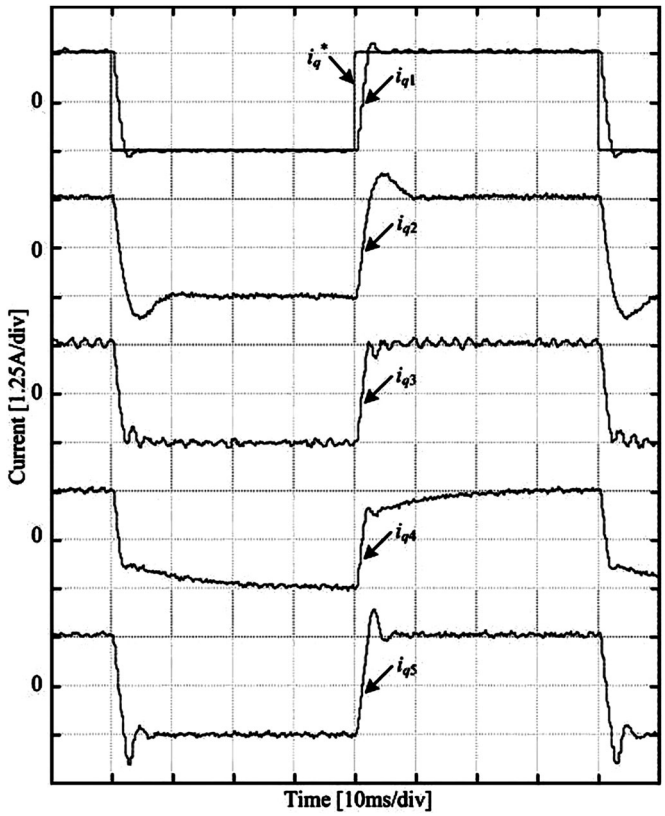

Fig. 5. Step test results of PI control with different K_P and K_I.

TABLE II
CORRESPONDING PI PARAMETERS OF DIFFERENT CURVES

Curve	i_{q1}	i_{q2}	i_{q3}	i_{q4}	i_{q5}
K_P	5	2	10	5	5
K_I	0.1	0.1	0.1	0.02	0.2

It is obvious that the integral action makes a zero tracking error, and the gain K_I decides how soon the actual current reaches the steady state. Therefore, the PI control requires a complicated regulation process before the optimal gains are obtained, and an overshoot phenomenon is inevitable on account of a high-dynamic requirement.

Additionally, for the same set of PI parameters, the tracking performance is different with the variation of the control command. Fig. 6 shows the step tracking test for different control commands. If the command amplitude changes from 1.25 to 2.5 A, for the same set of parameters $(K_P = 5, K_I = 0.1)$, it is clear that the actual current takes more time to reach the steady state when the command is 2.5 A, and the curve likes i_{q4} in Fig. 5, the gain K_I is smaller than the optimal value. Therefore, though PI control is a sample and practical method, it has some limitations in high-performance applications.

To improve the current tracking performance, the predictive control method is studied in this paper. However, the time-delay issue will introduce a large overshoot and oscillation, as shown in Fig. 7.

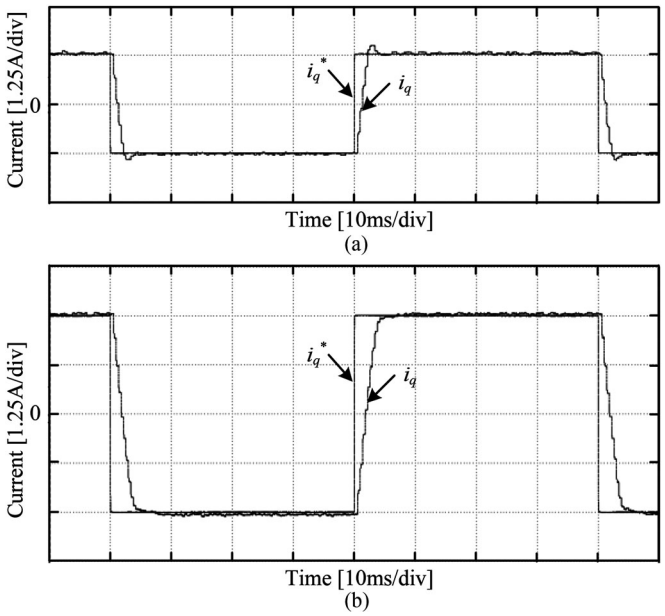

Fig. 6. Step test for different command amplitudes with the same PI parameters ($K_P = 5, K_I = 0.1$). (a) 1.25 A. (b) 2.5 A.

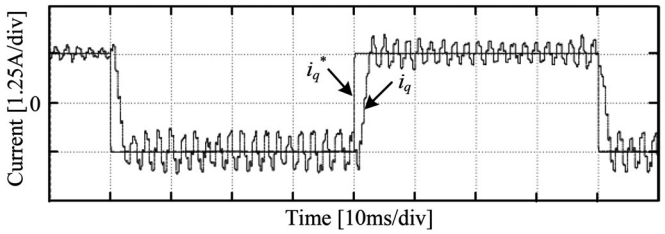

Fig. 7. PCC method without the time-delay compensation.

Hence, two sampling periods are used to implement the proposed PCC by the description of Section III. Fig. 8 shows the proposed PCC methods for different command amplitudes. Obviously, the oscillation phenomenon disappears; more over, the actual current tracks its command value precisely without the overshoot and steady-state error, and compared with Fig. 6, the tracking performance is not affected by the variation of the control command. In short, the proposed PCC has a better control performance than the PI control.

To express the robustness of the proposed PCC scheme, experiments about the parameter mismatch between the controller and motor are carried out. Because the modification of motor parameter is inconvenient, the corresponding research is implemented by changing the controller parameters.

Fig. 9 shows the control performance under the resistance variation. The current command is set as $i_q^* = 1.25$ A at $t \geq 5$ ms. When the resistance value of the controller is 50% smaller than that of the motor, according to (2), the actual current without the compensation has a constant error than the command, as shown in Fig. 9(a). But for the proposed PCC method shown in Fig. 9(b), this error disappears, and the actual current tracks the command precisely.

Fig. 10 shows the control performance under the inductance variation. The current command is the same as Fig. 9. If the

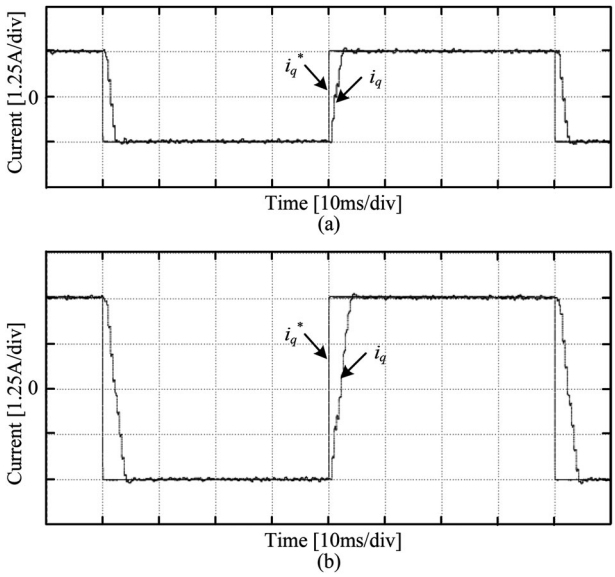

Fig. 8. Proposed PCC method for different command amplitudes. (a) 1.25 A. (b) 2.5 A.

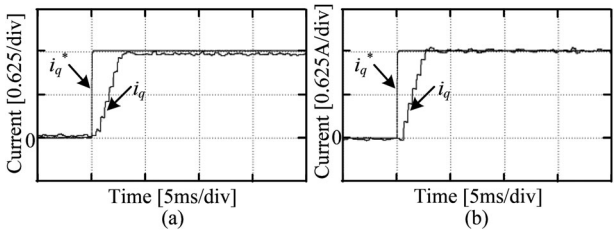

Fig. 9. Control performance under the resistance variation ($i_q^* = 1.25$ A). (a) Without the optimization. (b) With the optimization.

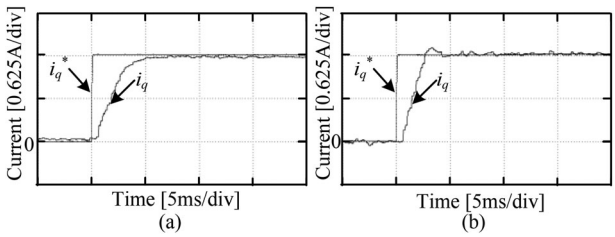

Fig. 10. Control performance under the inductance variation ($i_q^* = 1.25$ A). (a) Without the optimization. (b) With the optimization.

inductance value of the controller is 50% smaller than that of the motor, the dynamic performance of the PCC without the compensation will degrade. As shown in Fig. 10(a), the actual current rises slowly before it reaches the steady state. Fig. 10(b) shows the control performance with the proposed method. After the regulation, though a slight overshoot happens, the actual current tracks the command with a fast response, and the steady-state performance is not affected.

Fig. 11 shows the control performance under the magnetic flux variation. The current command is the same as Fig. 9. When the magnetic flux has a 50% decrease in the controller, the control performance without the optimization is shown in Fig. 11(a). It is clear that the actual q-axis current gradually diminishes as the increase of the velocity. The thrust reduction

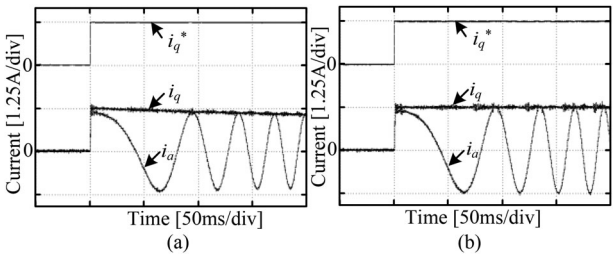

Fig. 11. Control performance under the magnetic flux variation ($i_q^* = 1.25$ A). (a) Without the optimization. (b) With the optimization.

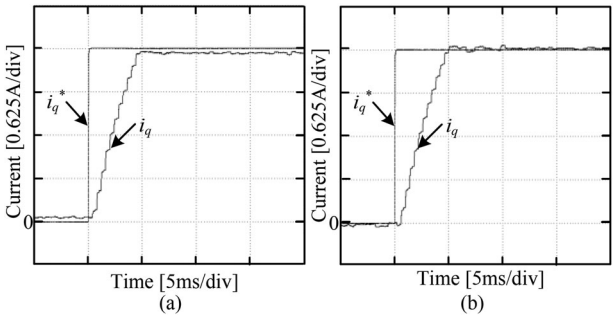

Fig. 12. Control performance under the resistance variation ($i_q^* = 2.5$ A). (a) Without the optimization. (b) With the optimization

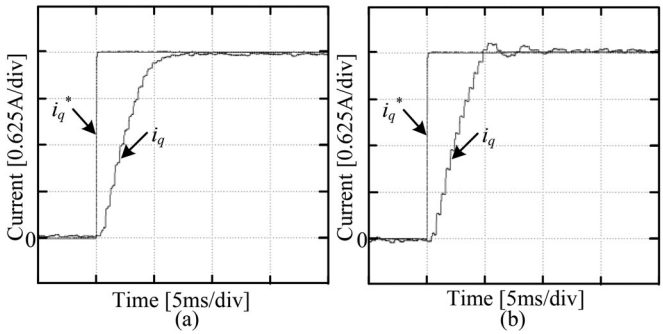

Fig. 13. Control performance under the inductance variation ($i_q^* = 2.5$ A). (a) Without the optimization. (b) With the optimization.

slows the accelerating process which can be seen through the stator current's trend. Fig. 11(b) shows the performance with the optimization. The problem caused by the magnetic flux variation is eliminated, and the regulation process is transitory and has no overshoot.

To adequately prove the correctness of the proposed PCC method, the command amplitudes in Figs. 9–11 are changed from 1.25 to 2.5 A, and other conditions are invariant; the corresponding experiments are implemented as follows. Figs. 12–14 are the control performance under the resistance, inductance, and magnetic flux variation, respectively. As expected, the performance of the optimal PCC method is not affected by the variation of the command after the adjustment. In conclusion, the proposed PCC method not only solves the overshoot and oscillation problem caused by the time delay, but also the parameter variation issue is overcome at the same time, and the

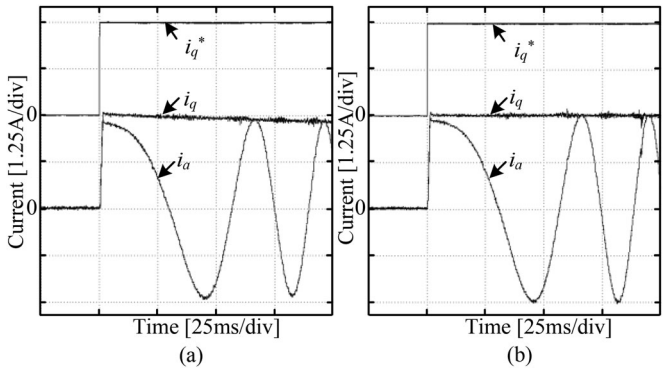

Fig. 14. Control performance under the magnetic flux variation ($i_q^* = 2.5$ A). (a) Without the optimization. (b) With the optimization.

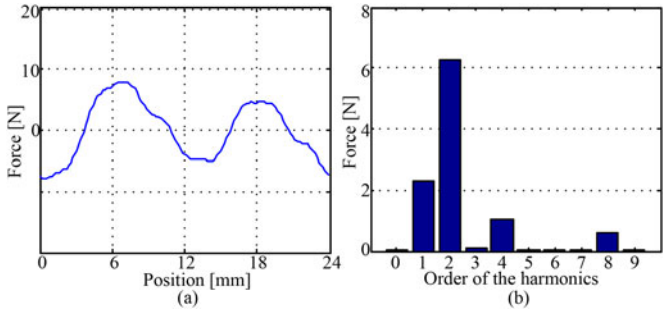

Fig. 15. Thrust ripple analysis by the FEM. (a) Ripple waveform. (b) Frequency spectrum analysis.

bandwidth and robustness of the current loop are improved by this simple and feasible scheme.

To evaluate the feasibility of the proposed thrust ripple suppression scheme, first, the main harmonic components of thrust ripple are analyzed by the FEM. Second, a comparison bet ween the measured and estimated ripple force is made to prove that the presented linearization observer can effectively estimate the thrust ripple, and then experimental results of estimated harmonic components are shown. Finally, tests on the velocity tracking performance are carried out. The velocity loop is implemented by a PI controller, and the current loop is regulated by the proposed PCC with the linearization observer.

Fig. 15 shows the analysis result of the thrust ripple through the FEM. It is clear that the ripple has a wide spectrum distribution. Taking a pair of pole pitch ($2\tau = 24$ mm) as one cycle, though the dominant harmonic components are the fundamental- and second-order harmonics, the relative high-frequency components such as the fourth- and eighth-order also account for a certain proportion. The amplitude of these four harmonics is 2.29, 7.46, 1.01, and 0.6 N, respectively.

Fig. 16 shows the comparison result between the measured and estimated thrust ripple with a low and constant velocity of 0.1 m/s. It can be seen that the actual thrust ripple is not completely periodic; hence, the compensation depending on the FEM is unreasonable. Because other assistive equipments and harsh environmental condition are required, the method by the experimental measurement is inconvenient. However, the real-time observation technology has an enormous advantage in

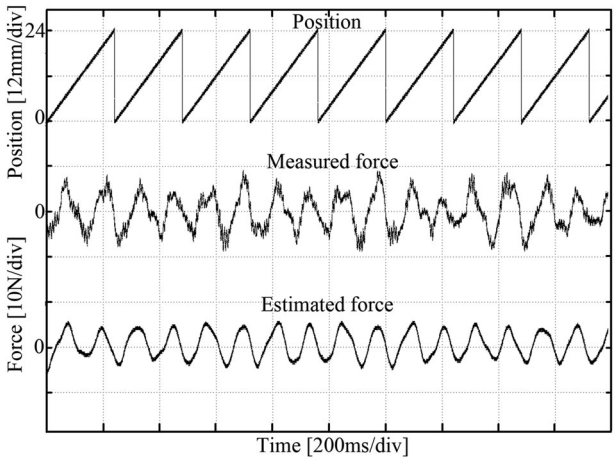

Fig. 16. Comparison result between the measured and estimated thrust ripple.

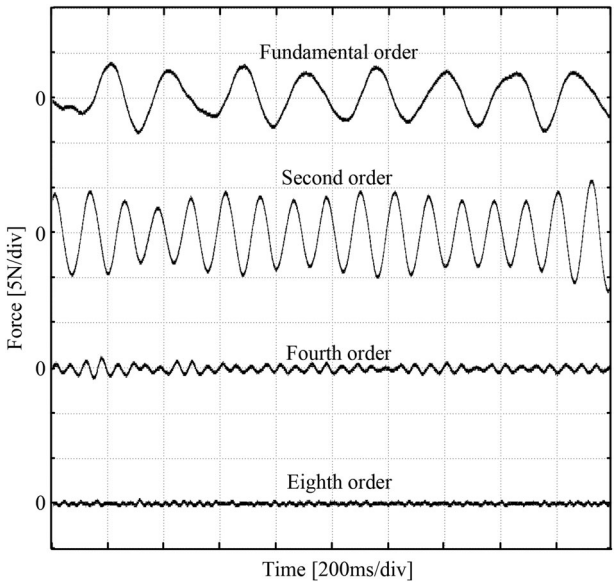

Fig. 17. Estimated results of main harmonic components.

suppressing the thrust ripple. In Fig. 16, though the restriction on the convergent speed of the proposed algorithm produces a slight deviation between the estimated and measured force, the estimated ripple force has a close approximation with the measured value. Therefore, the designed observer is suitable for the thrust ripple compensation.

Fig. 17 shows the main harmonic components. It is apparent that the most prominent contributions to the ripple force are the fundamental- and second-order harmonics, and the fourth- and eighth-order ones also exist. The amplitude from low- to high-order harmonic is about 6.2, 7.5, 1.2, and 0.6 N, respectively. Due to constant offsets of the measured currents produced by current sensors, the amplitude of the estimated fundamental-order harmonic is larger than the actual value. Hence, the proposed observer can effectively estimate the thrust ripple.

Due to the existence of the ripple force, the actual velocity has a certain ripple under the velocity closed loop condition. Fig. 18 shows the velocity step test without or with the ripple

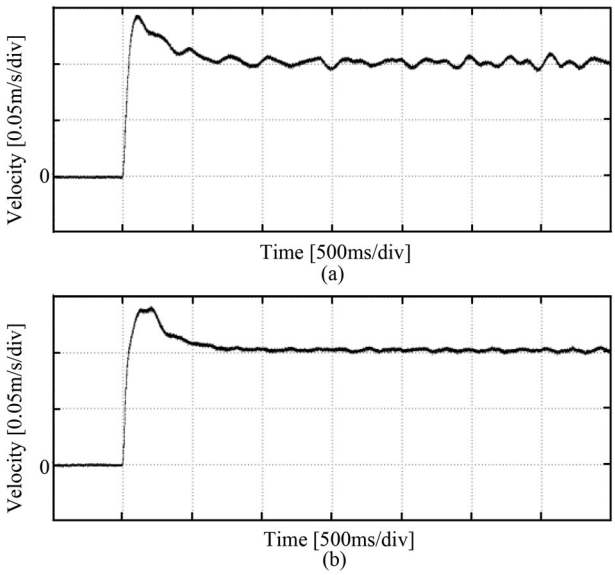

Fig. 18. Experimental results of the velocity response. (a) Without the ripple suppression. (b) With the ripple suppression.

suppression. To clearly express the velocity fluctuation caused by the thrust ripple, a low-velocity command and bandwidth are designed. The velocity command is given as 0.1 m/s at $t \geq 500$ ms. Fig. 18(a) shows the tracking result without the suppression. The velocity fluctuation is about 4%. However, through the compensation of the presented linear observer, as shown in Fig. 18(b), the fluctuation rate is below 1%, which confirms that the thrust ripple can be suppressed significantly.

VI. Conclusion

This paper has studied the high-performance current regulation scheme for PMLSM drives based on an optimal PCC method. Meanwhile, the thrust ripple has been compensated by using a novel linearization observer. Unlike PI control, the proposed PCC has a better dynamic and static performance even if the command changes. Compared with the conventional PCC, besides the time-delay compensation, the presented method does not require an extra design to eliminate the parameter disturbance, thus these two issues can be simultaneously overcome by a simple and practical strategy. The actual current can precisely track the command value after two sampling periods, and the current loop has advantages of the high-bandwidth and strong robust. In addition, the undesirable current component corresponding to the thrust ripple is diminished by the presented compensation scheme. Refer to the ripple obtained by the finite-element analysis or experimental measurement, the proposed observer can effectively estimate the ripple in real time. After the ripple suppression, the influence of the thrust ripple on the velocity response can be minimized. Based on a precise PMLSM test platform, the proposed current regulation scheme is realized by using a full digital control system, and its effectiveness is verified by the comparative experiments.

In summary, the main contribution of this paper is to present an efficient current control strategy that is appropriate for the PMLSM, and the thrust ripple specific to the linear motor is suppressed by the linearization observer. The proposed scheme pays attention to the practicability and conciseness, and avoids the infeasible and complex algorithm. In future work, though this paper can simultaneously resolve issues on the time delay and parameter variation in the PCC, we intend to study an improved predictive control which can also suppress the thrust ripple, then further increase the integration level of the current control scheme.

REFERENCES

[1] F. J. Lin, J. C. Hwang, P. H. Chou, and Y. C. Hung, "FPGA-based intelligent-complementary sliding-mode control for PMLSM servo-drive system," *IEEE Trans. Power Electron.*, vol. 25, no. 10, pp. 2573–2587, Oct. 2010.

[2] Y. S. Kung, C. C. Huang, and M. H. Tsai, "FPGA realization of an adaptive fuzzy controller for PMLSM drive," *IEEE Trans. Ind. Electron.*, vol. 56, no. 8, pp. 2923–2932, Aug. 2009.

[3] Y. S. Kung, "Design and implementation of a high-performance PMLSM drives using DSP chip," *IEEE Trans. Ind. Electron.*, vol. 55, no. 3, pp. 1341–1351, Mar. 2008.

[4] W. T. Su and C. M. Liaw, "Adaptive positioning control for a LPMSM drive based on adapted inverse model and robust disturbance observer," *IEEE Trans. Power Electron.*, vol. 21, no. 2, pp. 505–517, Mar. 2006.

[5] F. J. Lin, L. T. Teng, and H. Chu, "A robust recurrent wavelet neural network controller with improved particle swarm optimization for linear synchronous motor drive," *IEEE Trans. Power Electron.*, vol. 23, no. 6, pp. 3067–3078, Nov. 2008.

[6] D. H. Zhou, J. Zhao, and Y. Liu, "Predictive torque control scheme for three-phase four-switch inverter-fed induction motor drives with DC-link voltages offset suppression," *IEEE Trans. Power Electron.*, vol. 30, no. 6, pp. 3309–3318, Jun. 2015.

[7] Y. A.-R. I. Mohamed and E. F. El-Saadany, "Robust high bandwidth discrete-time predictive current control with predictive internal model—A unified approach for voltage-source PWM converters," *IEEE Trans. Power Electron.*, vol. 23, no. 1, pp. 126–136, Jan. 2008.

[8] C. K. Lin, T. H. Liu, M. Y. Wei, L. C. Fu, and C. F. Hsiao, "Model-free predictive current control for interior permanent-magnet synchronous motor drives based on current difference detection technique," *IEEE Trans. Ind. Electron.*, vol. 61, no. 2, pp. 667–681, Feb. 2014.

[9] L. H. Zhang, B. Gu, J. Dominic, B. F. Chen, C. Zheng, and J. S. Lai, "A dead-time compensation method for parabolic current control with improved current tracking and enhanced stability range," *IEEE Trans. Power Electron.*, vol. 30, no. 7, pp. 3892–3902, Jul. 2015.

[10] D.-C. Lee, S.-K. Sul, and M.-H. Park, "High performance current regulator for a field-oriented controlled induction motor drive," *IEEE Trans. Ind. Appl.*, vol. 23, no. 5, pp. 1247–1257, Sep./Oct. 1994.

[11] M. Comanescu, L. Y. Xu, and T. D. Batzel, "Decoupled current control of sensorless induction-motor drives by integral sliding mode," *IEEE Trans. Ind. Electron.*, vol. 55, no. 11, pp. 3836–3845, Nov. 2008.

[12] M. Boussak and K. Jarray, "A high-performance sensorless indirect stator flux orientation control of induction motor drive," *IEEE Trans. Ind. Electron.*, vol. 53, no. 1, pp. 41–49, Feb. 2006.

[13] L. Harnefors and H.-P. Nee, "Model-based current control of AC machines using the internal model control method," *IEEE Trans. Ind. Appl.*, vol. 34, no. 1, pp. 133–141, Jan./Feb. 1998.

[14] S.-M. Hwang, K.-T. Kim, W.-B. Jeong, Y.-H. Jung, and B.-S. Kang, "Comparison of vibration sources between symmetric and asymmetric HDD spindle motors with rotor eccentricity," *IEEE Trans. Ind. Appl.*, vol. 37, no. 6, pp. 1727–1731, Nov./Dec. 2001.

[15] H.-T. Moon, H.-S. Kim, and M.-J. Youn, "A discrete-time predictive current control for PMSM," *IEEE Trans. Power Electron.*, vol. 18, no. 1, pp. 464–472, Jan. 2003.

[16] J. Weigold and M. Braun, "Predictive current control using identification of current ripple," *IEEE Trans. Ind. Electron.*, vol. 55, no. 12, pp. 4346–4353, Dec. 2008.

[17] D.-C. Lee, S.-K. Sul, and M.-H. Park, "High performance current regulator for a field-oriented controlled induction motor drive," *IEEE Trans. Ind. Appl.*, vol. 30, no. 5, pp. 1247–1257, Sep./Oct. 1994.

[18] W. N. Mohamed, A. N. Ahmad, M. Eric, and S. -B. Ilhem, "FPGA-based predictive current controller for synchronous machine speed drive," *IEEE Trans. Power Electron.*, vol. 23, no. 4, pp. 2115–2126, Jul. 2008.

[19] H. L. Huy, K. Slimani, and P. Viarouge, "Analysis and implementation of a real-time predictive current controller for permanent-magnet synchronous servo drives," *IEEE Trans. Ind. Electron.*, vol. 41, no. 1, pp. 110–117, Feb. 1994.

[20] K.-W. Kim and M.-J. Youn, "A simple and robust digital current control technique of a PM synchronous motor using time delay control approach," *IEEE Trans. Power Electron.*, vol. 16, no. 1, pp. 72–82, Jan. 2001.

[21] K.-H. Kim, "Model reference adaptive control-based adaptive current control scheme of a PM synchronous motor with an improved servo performance," *IET Electr. Power. Appl.*, vol. 3, no. 1, pp. 8–18, Jan. 2009.

[22] P. Wipasuramonton, Z. Q. Zhu, and D. Howe, "Predictive current control with current-error correction for PM brushless AC drives," *IEEE Trans. Ind. Appl.*, vol. 42, no. 4, pp. 1071–1079, Jul./Aug. 2006.

[23] S.-J. Jeong and S.-H. Song, "Improvement of predictive current control performance using online parameter estimation in phase controlled rectifier," *IEEE Trans. Power Electron.*, vol. 22, no. 5, pp. 1820–1825, Sep. 2007.

[24] S. Kwak, U.-C. Moon, and J.-C. Park, "Predictive-control-based direct power control with an adaptive parameter identification technique for improved AFE performance," *IEEE Trans. Power Electron.*, vol. 29, no. 11, pp. 6178–6187, Nov. 2014.

[25] K. Sato, "Thrust ripple reduction in ultrahigh-acceleration moving-permanent-magnet linear synchronous motor," *IEEE Trans. Magn.*, vol. 48, no. 12, pp. 4866–4873, Dec. 2012.

[26] J. G. Amoros and P. Andrada, "Sensitivity analysis of geometrical parameters on a double-sided linear switched reluctance motor," *IEEE Trans. Ind. Electron.*, vol. 57, no. 1, pp. 311–319, Jan. 2010.

[27] Y.-W. Zhu, D.-H. Koo, and Y.-H. Cho, "Detent force minimization of permanent magnet linear synchronous motor by means of two different methods," *IEEE Trans. Magn.*, vol. 44, no. 11, pp. 4345–4348, Nov. 2008.

[28] J.-J. Cai, Q.-F. Lu, X.-Y. Huang, and Y.-Y. Ye, "Thrust ripple of a permanent magnet LSM with step skewed magnets," *IEEE/ASME Trans. Magn.*, vol. 48, no. 11, pp. 4666–4669, Nov. 2012.

[29] P. Van Den Braembussche, J. Swevers, H. Van Brussel, and P. Vanherck, "Accurate tracking control of linear synchronous motor machine tool axes," *Mechatronics*, vol. 6, no. 5, pp. 507–521, Aug. 1996.

[30] L. Bascetta, P. Rocco, and G. A. Magnani, "Force ripple compensation in linear motors based on closed-loop position-dependent identification," *IEEE/ASME Trans. Mechatronics*, vol. 15, no. 3, pp. 349–359, Jun. 2010.

[31] W. Qian, S. K. Panda, and J.-X. Xu, "Torque ripple minimization in PM synchronous motors using iterative learning control," *IEEE Trans. Power Electron.*, vol. 19, no. 2, pp. 272–279, Mar. 2004.

[32] P. Mattavelli, L. Tubiana, and M. Zigliotto, "Torque-ripple reduction in PM synchronous motor drives using repetitive current control," *IEEE Trans. Power Electron.*, vol. 20, no. 6, pp. 1423–1431, Nov. 2005.

[33] T. S. Hwang and J. K. Seok, "Observed-based ripple force compensation for linear hybrid stepping motor drives," *IEEE Trans. Ind. Electron.*, vol. 54, no. 5, pp. 2417–2424, Oct. 2007.

[34] C.-H. Ting and Y.-N. Chang, "Observer-based backstepping control of linear stepping motor," *Control Eng. Pract.*, vol. 21, no. 7, pp. 930–939, Jul. 2013.

[35] N. H. Jo and J. H. Seo, "State observer for nonlinear systems and its application to ball and beam system," *IEEE Trans. Autom. Control*, vol. 45, no. 5, pp. 968–973, May 2000.

Mingyi Wang was born in Jilin, China. He received the B.E. and M.E. degrees in electrical engineering from the Harbin Institute of Technology (HIT), Harbin, China, in 2009 and 2011, respectively, where he is currently working toward the Ph.D. degree at the Institute of Electromagnetic and Electronic Technology.

His research interests include motor drive control, power electronic applications, and magnetic levitation.

Liyi Li (M'09) received the B.E., M.E., and D.E. degrees from the Harbin Institute of Technology (HIT), Harbin, China, in 1991, 1995, and 2001, respectively.

Since 2004, he has been a Professor with the School of Electrical Engineering and Automation, HIT. He has authored or coauthored more than 110 technical papers and is the holder of 50 patents. His research interests include control and drive of linear motors, linear electromagnetic launch, accumulation of electric energy, and superconducting motors.

Donghua Pan received the B.E. and M.E. degrees from the Shenyang University of Technology, Shenyang, China, in 2005 and 2008, respectively, and the Ph.D. degree from the Harbin Institute of Technology, Harbin, China, in 2013.

He is currently with the Research Center of Basic Space Science, Harbin Institute of Technology. His current research interests include linear permanent-magnet synchronous motors and zero magnetic field facility.

Yongbin Tang was born in Hunan, China. He received the M.E. and Ph.D. degrees in electrical engineering from the Harbin Institute of Technology, Harbin, China, in 2009 and 2014, respectively.

He is currently with the Institute of Automatic Control Equipment, Beijing, China. His research interests include motor design, servo mechanism, and robot applications.

Qingbo Guo was born in Harbin, China. He received the B.E. and M.E. degrees in electrical engineering from the Harbin Institute of Technology, Harbin, China, in 2010 and 2012, respectively, where he is currently working toward the Ph.D. degree at the Institute of Electromagnetic and Electronic Technology.

His research interests include motor drive control and power electronic applications.